Advanced Functional Materials

ADVANCED FUNCTIONAL MATERIALS
www.afm-journal.de

RESEARCH ARTICLE

Anisotropic Strain-Induced Piezoelectric Polarization in 3R-MoS_2 for Enhanced Piezo-Photocatalytic Oxidation of Formaldehyde

Weina Zhao[1,2] | Chang Shen[1,2] | Xinyue Fang[1,2] | Shengnan Song[1,2] | Jinlong Wang[1,2] | Yunlong Guo[1,2] | Shengcai Zhu[3] | Jukun Xiong[1,2] | Guiying Li[1,2] | Taicheng An[1,2]

[1]Guangdong Key Laboratory of Environmental Catalysis and Health Risk Control, Guangdong-Hong Kong-Macao Joint Laboratory for Contaminants Exposure and Health, Institute of Environmental Health and Pollution Control, Guangdong University of Technology, Guangzhou, China | [2]Guangdong Basic Research Center of Excellence for Ecological Security and Green Development, Guangzhou Key Laboratory of Environmental Catalysis and Pollution Control, School of Environmental Science and Engineering, Guangdong University of Technology, Guangzhou, China | [3]School of Materials, Shenzhen Campus of Sun Yat-Sen University, Shenzhen, China

Correspondence: Taicheng An (antc99@gdut.edu.cn)

Received: 28 October 2025 | **Revised:** 6 December 2025 | **Accepted:** 11 December 2025

Keywords: DFT calculations | formaldehyde oxidation | photocatalytic oxidation | piezoelectric polarization

ABSTRACT

The efficient removal of formaldehyde (HCHO), a pervasive and hazardous atmospheric pollutant, remains challenging due to inherent limitations in conventional photocatalysis, particularly rapid charge recombination and insufficient reactive oxygen species (ROS) generation. Although the non-centrosymmetric structure of sliding ferroelectric 3R-MoS_2 enables piezoelectric polarization to overcome these constraints, the atomistic origin of how this anisotropic strain-induced polarization modulates surface reaction kinetics is not well understood. Herein, we develop a first-principles piezoelectric polarization model and integrate it with experimental validation to unravel the atomic-scale piezo-photocatalytic mechanism of 3R-MoS_2 for HCHO degradation. Our results demonstrate that anisotropic compressive strain along the armchair direction induces strong piezoelectric polarization via asymmetric Mo—S displacements, while zigzag-oriented strain produces negligible response. Experimental characterization confirms the successful synthesis of the non-centrosymmetric 3R-MoS_2 and its pronounced anisotropy. The tailored polarization establishes an internal electric field that simultaneously optimizes band structure and aligns with critical redox potentials for efficient charge separation. Remarkably, −6% armchair polarization reduces the energy barrier of the rate-determining step by 92% through interfacial charge redistribution and d-band center upshift. Experimental validation confirms a twofold catalytic enhancement in 3R-MoS_2 over the 2H-phase. This work elucidates strain-directed piezo-photocatalytic HCHO oxidation and paves the way for noble-metal-free environmental remediation.

1 | Introduction

Formaldehyde (HCHO), as a ubiquitous indoor and industrial air pollutant, poses severe threats to both environmental safety and public health [1–4]. It is thus of critical importance to develop highly efficient strategies for HCHO removal at ambient temperature [5, 6]. While conventional approaches such as adsorption, plasma systems, and thermal catalytic oxidation are widely used, their practical application is often hampered by limitations including high energy consumption, the potential for secondary pollution, or inadequate efficiency under ambient conditions [7, 8]. In contrast, photocatalytic oxidation has gained

particular scientific prominence owing to its unique combination of operational simplicity, relatively mild reaction conditions, and capacity for complete mineralization of HCHO into harmless products, thereby establishing it as a promising strategy for sustainable HCHO control [9–11].

The photocatalytic process begins with light-triggered generation ($h\nu$) of electron–hole pairs (e^-/h^+) within a semiconductor catalyst, followed by the key step of reactive oxygen species (ROSs) formation driven by these charge carriers. These ROSs mediate radical reactions that ultimately mineralize adsorbed volatile organic compounds into H_2O and CO_2 [12]. Despite its potential, photocatalytic HCHO oxidation remains hampered by rapid charge carrier recombination and insufficient ROSs generation, which concertedly limit quantum efficiency and overall oxidation performance. Advancing this technology, therefore, hinges on sophisticated material design strategies including elemental doping, oxygen vacancy engineering, plasmonic integration, and heterojunction construction with all engineered to optimize charge dynamics and maximize electron–hole separation [13, 14]. For instance, Kuk et al. [10] developed a BiOI/TiO_2 p-n junction photocatalyst where mobile singlet oxygen ($^1O_2$) served as the dominant ROS for efficient HCHO degradation. Separately, Wang et al. [11] synthesized a multifunctional $BaTiO_3$/g-C_3N_4/PTFE/Cu thin film via hydrothermal method, also for HCHO photocatalytic degradation. These composites exhibited highly efficient and stable degradation of airborne formaldehyde under solar irradiation conditions. However, the concurrent optimization of charge separation kinetics and catalytic performance under ambient conditions remains a critical challenge, rooted in the inherent limitations of conventional photocatalysts, such as suboptimal band structures and inefficient charge dynamics [15, 16]. Addressing this multifaceted problem, therefore, demands breakthrough strategies capable of orchestrating both bulk charge transport and surface reaction kinetics.

Recently, piezoelectric engineering has emerged as a pivotal strategy to address the long-standing challenge of charge recombination in photocatalysis by leveraging controllable strain-induced polarization [17]. Arising from stress-induced lattice distortion and charge polarization in the unique non-centrosymmetric crystalline architectures, these piezoelectric materials develop an internal piezoelectric field with spatially separated electron–hole domains, enabling the simultaneous enhancement of photogenerated charge separation and precise band structure modulation [18]. Under mechanical stress, the resulting piezoelectric potential orchestrates directional charge migration across catalytic interfaces while synergistically intensifying carrier dynamics, thereby establishing a coherent bridge between mechanical energy and photocatalytic redox cycles [19]. For example, Yuan et al. [20] synthesized Cl-doped ZnO nanorods (Cl—ZnO NRs) to employ piezoelectric effects for band structure tuning and energy harvesting, thereby enhancing the photocatalytic degradation of dyes. Similarly, He et al. [21] produced $BiFeO_3$ nanosheets via a solvothermal method and utilized piezoelectric polarization to overcome the intrinsic activity limitations of perovskite photocatalysts. In another study, Chen et al. [22] discovered that MoS_2 monolayer can generate a piezoelectric field on its surface, which can improve charge separation and enhance piezoelectric catalytic performance. These studies collectively confirm that the polarization effect in piezoelectric semiconductors can enhance photocatalytic performance.

As an emerging sliding ferroelectric, the noncentrosymmetric 3R phase of MoS_2 has attracted considerable interest as a piezoelectric semiconductor due to its unique combination of strain-responsive polarization and intrinsic visible-light absorption, while leveraging its earth-abundant and non-noble metal sustainability [23]. Unlike conventional centrosymmetric polymorphs, 3R-MoS_2 exhibits a unique ABC-type interlayer stacking configuration [24] that breaks inversion symmetry, enabling efficient mechano-electric coupling where mechanical stresses directly induce coordinated atomic displacements that generate directional charge polarization across crystal planes [25, 26]. In addition, 2D architectures have emerged as a highly promising piezoelectric material system due to their exceptional structural advantages, including the elevated specific surface area, superior charge transport characteristics, as well as the remarkable mechanical flexibility that enables sustained operation under substantial strains [27, 28]. This distinctive feature, coupled with its high active-site density and tunable electronic structure, positions 3R-MoS_2 as an ideal platform for synergistically enhancing photocatalytic performance through photopiezoelectric coupling [29]. For instance, Cai et al. [30] constructed a flexible *p–n* heterojunction by mechanically stacking α-In_2Se_3 and 3R-MoS_2 flakes onto a polyimide substrate. They observed a notable increase in photocurrent under tensile strain, which they attributed to strain-induced piezoelectric polarization that effectively modulates the interfacial band alignment. Despite demonstrating that piezoelectric polarization enhances photocatalytic degradation performance [31, 32], the majority of these investigations primarily focus on material modifications, yet the atom-scale synergistic mechanism mediating formaldehyde degradation remains elusive. Specifically, a fundamental understanding of how the strain direction and magnitude modulate piezoelectric polarization in 3R-MoS_2 and subsequently dictate surface reaction energetics and pathways is lacking, thus making it imperative to establish the underlying structure-activity relationship at the atomic scale.

To bridge this gap, we develop a piezoelectric polarization model via first-principles calculations to unravel the piezoelectric-photocatalytic synergistic mechanism in HCHO degradation on 3R-MoS_2. A multiscale modeling approach combining large-scale density functional theory (DFT) with an implicit periodic continuum model was adopted to simulate the interfacial reaction environment at the solid–gas interface. We first evaluate the structural stability of 3R-MoS_2 under strain and quantify the strain-direction (armchair vs. zigzag)/ magnitude dependence of its piezoelectric response, electronic band structure, and charge redistribution. Subsequently, we combined calculations of spontaneous polarization intensity, redox capability, and transition state theory to elucidate how piezoelectric polarization regulates key reaction descriptors, including hydroxyl radical (·OH) generation, reaction energy barriers, and d-band center shifts, and identified an optimal strain threshold (–6%) for maximizing HCHO oxidation kinetics. Ultimately, by combining theoretical modeling with experimental validation, this work not only elucidates how piezoelectric polarization dictates the photocatalytic degradation of formaldehyde but also provides a theoretical basis for applying external strain to 3R-MoS_2 to achieve highly efficient VOC mineralization.

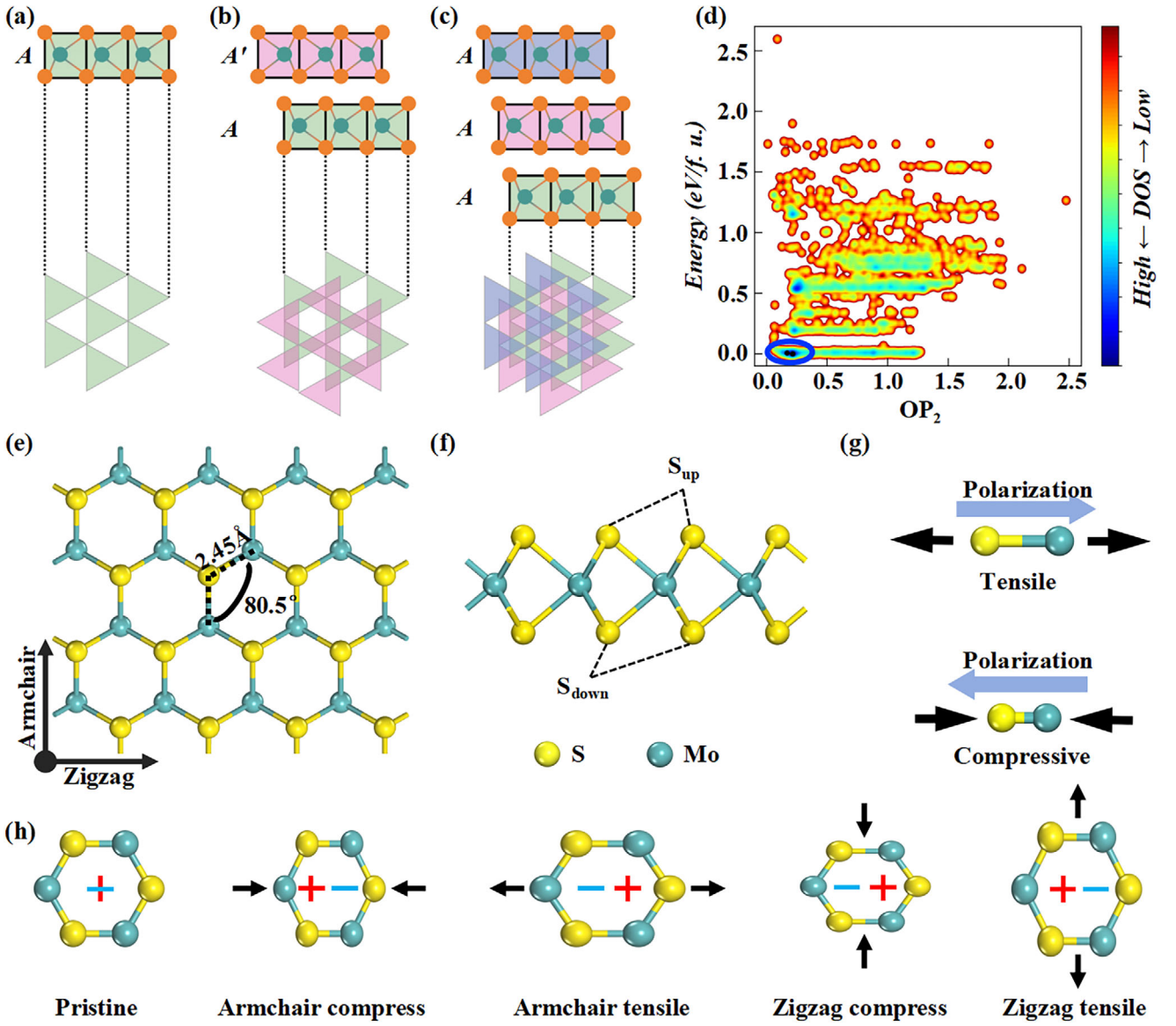

FIGURE 1 | (a–c) Side and top view of the 1H, 2H and 3R MoS_2 stackings, respectively. (d) Illustration of global PES for MoS_2 using the OP_2-E contour plot, as enlarged from the same plot (the inset black dots) identified from the total dataset from the SSW-NN simulation. OP_2: the structural order parameter with $l = 2$ (Equation 1). The energy of the GM (2H-MoS_2 phase) is set as energy zero. (e,f) Top and side views of the optimized geometries of 3R-MoS_2 monolayer. The yellow and blue sphere represent the S atom and Mo atom, respectively (the same below). (g) Schematic diagram of polarization generation in tensile and compression direction. (h) The charge distribution of 3R-MoS_2 under strain.

2 | Results and Discussion

2.1 | Phase Stability and Piezoelectric Polarization Model of 3R-MoS_2

2.1.1 | Energetics and Phase Stability of 3R-MoS_2

Figure 1a–c illustrates the structural configurations of three predominant MoS_2 polymorphs: 1H, 2H, and 3R phases, all of which were characterized by trigonal prismatic coordination geometry. As demonstrated in Table 1, the 1H phase exhibited a monolayer S—Mo—S sandwich structure (hexagonal system) with in-plane lattice constants a = b = 3.16 Å, monolayer thickness 6.15 Å, and space group *P*6_m2 (No. 187, D_3h symmetry). The 2H phase is formed by AB-stacked bilayers of 1H units (hexagonal system) with lattice parameters a = b = 3.16 Å, c = 12.30 Å, and space group $P6_3/mmc$ (No. 194, D_6h symmetry) [33–35]. In contrast, the 3R phase exhibited a three-layer repeating sequence of 1H configurations, while adopting a rhombohedral structure with the experimental lattice parameters of (a = b = 3.16 Å, and c = 18.37 Å), crystallizing in the non-centrosymmetric space group R_3m (No. 160, C_3v symmetry) [36]. Notably, Suzuki et al. [37]. have experimentally demonstrated spin polarization phenomena in these systems, highlighting their unique electronic properties arising from distinct structural symmetries.

A search was conducted of three common crystal phases, 1H, 2H, and 3R, resulting in the identification of five structures, as illustrated in Figure 1a–c and Figure S1. In Figure 1d, the first-principles derived OP_2-E contour map of the global structural

TABLE 1 | The structural parameters and spatial symmetry of 1H-, 2H-, and 3R-MoS_2 polytypes.

Phase structure	Lattice parameter	Crystal system	Space group	Ref.
1H	a = b = 3.16 Å c = 6.15Å	hexagonal	*P*6_m2 (No. 187, D_3h)	[39–41]
2H	a = b = 3.16 Å c = 12.30 Å	hexagonal	$P6_3/mmc$ (No. 194, D_6h)	[39–41]
3R	a = b = 3.16 Å c = 18.37 Å	rhombohedral	R_3m (No. 160, C_3v)	[42]

dataset was displayed, where the experimentally identified configurations (black dots) were localized at the minima of the global PES, highlighting their intrinsic electronic properties. It illustrates that the OP_2 values of the five structures are proximate, exhibiting a comparable energy profile, thereby indicating a similar degree of stability. The 1H phase demonstrates metallic conductivity, rendering it particularly effective for electrocatalytic applications, while both 2H- and 3R-MoS_2 exhibited semiconductor characteristics with appropriate bandgap energies, positioning them as prime candidates for photocatalytic systems. Crucially, 3R-MoS_2 distinguished itself through intrinsic piezoelectricity arising from its non-centrosymmetric atomic arrangement, a structural advantage absent in the 2H counterpart, that significantly enhances photo-mechanical coupling efficiency. Such a unique synergy of photoresponsive and piezoelectric functionalities underpins our selection of 3R-MoS_2 as the focal material for advanced photocatalyst development.

2.1.2 | Theoretical Modeling of Piezoelectric Polarization in 3R-MoS_2

The piezoelectric effect exhibits substantial sensitivity to structural deformations and vibrations, thereby rendering the surface atomic structure of the catalyst critically important in piezoelectric catalytic systems. Figure 1e,f presents the top and side perspectives of the optimized 3R-MoS_2 monolayer, which was modeled using a rhombohedral unit cell characterized by lattice parameters of (11.16 Å, 12.88 Å, 48 atoms). The vacuum spacing typically exceeded 20 Å. The optimized bond lengths and bond angles of Mo—S and S—Mo—S were 2.45 Å and 80.5° of MoS_2 monolayer, respectively. Additionally, the calculated bandgap of 3R-MoS_2 monolayer, determined using the hybrid Heyd–Scuseria–Ernzerhof (HSE06), was 2.07 eV, in comparison to the experimental value of 1.9 eV [31]. This suggests that 3R-MoS_2 monolayer is a promising piezoelectric-photocatalytic reactive intersurface, attributed to its substantial dielectric constant (the parallel E||x and perpendicular E||z directions are 4.95 and 2.92, respectively) [38] and suitable energy bandgap.

In the MoS_2 unit, depicted in Figure 1g, the application of tensile strain will lead to an increase in the interatomic distance between the Mo and S atoms. This alteration in relative positioning, coupled with the disparity in atomic charge, resulted in the polarization of the Mo atom. Conversely, the application of compressive strain will reduce the distance between the Mo and S atoms, thereby inducing polarization toward the S atom within the Mo—S unit. For 3R-MoS_2 monolayer, the polarization resulting from mechanical deformation arose from the superposition of the offset vector and the effective charge aligned along the offset direction of all constituent atoms. The computational methodology employed to derive this relationship is detailed in Equation 2. This phenomenon demonstrates that the application of strain can alter the relative positioning of Mo—S bonds and the charge distribution within the molecular layer of 3R-MoS_2. Consequently, a spontaneous piezoelectric polarization effect was induced, which subsequently influences the catalytic reaction.

Figure 1h provides a qualitative schematic representation of the piezoelectric properties of 3R-MoS_2, depicting the application of tensile stress in the armchair direction and compressive stress in the zigzag direction. Mechanical deformation along different orientations modified the relative positioning of Mo—S units, thereby inducing piezoelectric effects through the disruption of centrosymmetric phases and alteration of the overall charge distribution. In addition, we conducted a quantitative analysis of the variation in the piezoelectric effect along these two directions by employing the Born effective charge tensors (BECs) derived from 3R-MoS_2 calculations to estimate the spontaneous polarization intensity (Ps), as shown in Figure 2a. To mitigate the structural deactivation of MoS_2 resulting from substantial deformation rates, this study opted to impose a maximum external strain of 10% on MoS_2 along both the armchair and zigzag orientations [39]. It shows that the spontaneous polarization intensity along the zigzag direction remains approximately 0 C/m^2, regardless of the applied strain ratio. This phenomenon can be attributed to the absence of vector superposition between the charges on the Mo atom and the S atom, under both compressive and tensile strain conditions in the zigzag orientation. The opposite directions of atomic displacement, caused by the symmetry of the structure, lead to the mutual cancellation of dipole moments and the absence of a polarization effect. As illustrated in Figure 2b, the atomic displacement of the S_{down} and S_{up} atoms, relative to the centrosymmetric phase during compression, was equivalent in magnitude but occurred in opposite directions. The Mo atom underwent horizontal movement, remaining confined to the plane aligned with the direction of either stretching or compression, and thus does not exhibit displacement toward the vacuum layer. Notably, it is evident that the spontaneous polarization intensity was significantly greater in the armchair direction than in the zigzag direction. Furthermore, as the compression ratio increased, the spontaneous polarization intensity exhibited a progressive increase, reaching a maximum value of −0.14 C/m^2 at a compression ratio of 10%. As compressive strain intensifies, the atomic offset progressively deviated from the centrosymmetric

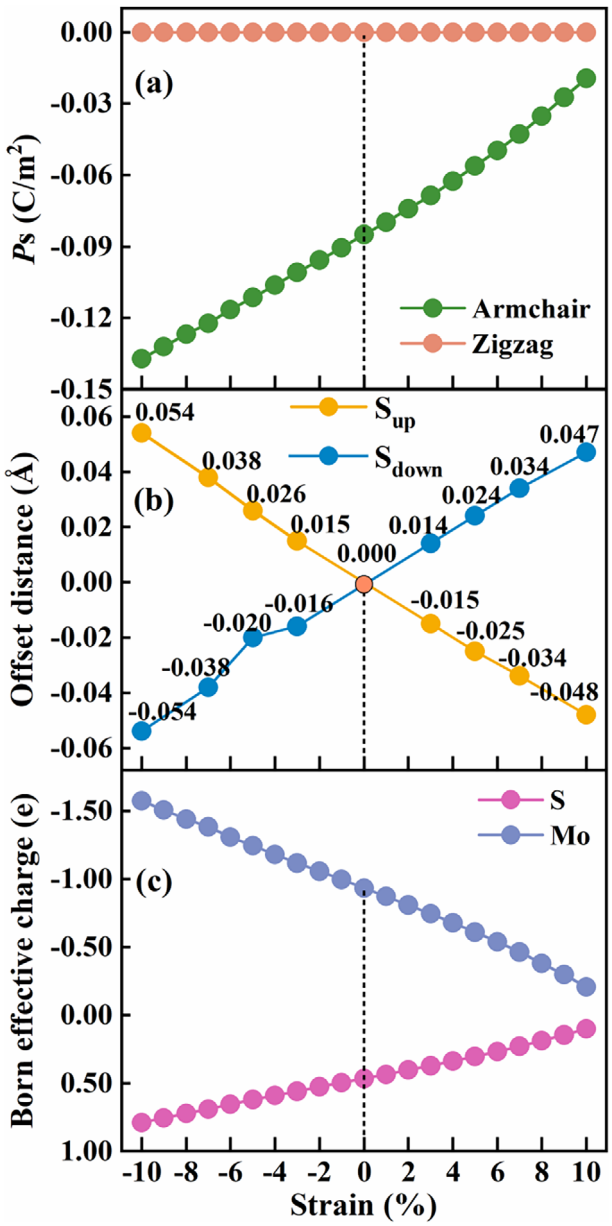

FIGURE 2 | (a) Spontaneous polarization intensity of 3R-MoS_2 in armchair and zigzag directions under different strain ratios; (b) The offset distance of the up row (S_{up}) and down row (S_{down}) of S atoms; (c) Born effective charges of S and Mo atoms in armchair directions under different strain ratios, where the negative sign indicates the opposite direction of the positive *x* axis.

reference term, leading to a corresponding increase in the piezoelectric polarization of the associated atoms.

To elaborate the relationship between charge strength and non-centrosymmetry in the 3R-MoS_2 unit cell, as well as to further investigate the intensity of spontaneous polarization, the calculated Born effective charges of S and Mo atoms obtained via DFT are presented in Figure 2c. The results indicate that compressive strain results in an increase in the Born effective charge as the compression ratio increases. Specifically, at a compression ratio of −10%, the atomic charge values for S and Mo reached −0.78 and 1.58 e, respectively. Conversely, the BEC of S and Mo atoms progressively approached zero as the tensile ratio increases, suggesting that the polarization effect induced by tensile strain is less pronounced compared to that of compressive strain. This phenomenon can be attributed to the opposite polarization responses of the material to different types of strain. Compressive strain enhances polarization as atomic displacement aligns with the BEC tensor, while tensile strain reduces polarization by increasing atomic spacing, which equalizes charge distribution and cancels dipole moments driving BEC toward zero.

2.2 | Piezopolarization Mediated ·OH Radical Generation on 3R-MoS_2

The production efficiency of ·OH, serving as a pivotal active species in photocatalytic degradation of VOCs [40], exhibits strong dependence on the band structure parameters of semiconductor catalysts, particularly their bandgap characteristics and band alignment [41]. To elucidate this structure-activity correlation, we thus initially quantified the strain-dependent bandgap evolution in 3R-MoS_2 under anisotropic mechanical loading along crystallographic orientations (Armchair vs. Zigzag), as schematized in Figure 3a. Notably, compressive strain induced a progressive expansion of the bandgap, reaching a maximum value of 2.38 eV at −5% strain. Conversely, tensile strain demonstrated an inverse trend, with the bandgap narrowing proportionally to increasing tensile deformation. The bandgap, representing the fundamental energy threshold required for electron excitation into the conduction band and subsequent participation in charge transfer processes [42–44], demonstrates that external strain application serves as an effective strategy for modulating electronic structure and energy states in MoS_2. Such mechanical tuning mechanism enables precise control over the material's photoelectronic properties critical for catalytic applications.

Subsequently, we computed the band edge positions of 3R-MoS_2 under varying strain ratios using Equations 5 and 6, with the results illustrated in Figure 3b,c. Along the armchair direction of 3R-MoS_2, under compressive strains ranging from −5% to −7% that simultaneously satisfy both ·OH/H_2O and O_2/·O_2^- redox potential requirements, the valence band edges were measured at 2.12, 2.09, and 2.05 eV, while the CB edges were −0.26, −0.26, and −0.26 eV, respectively. Under zigzag-direction compressive strains of −3% to −5%, 3R-MoS_2 achieved simultaneous alignment with the ·OH/H_2O and O_2/·O_2^- redox potentials. These results confirmed that compressive strain, irrespective of crystallographic orientation (armchair or zigzag), induced a threshold strain magnitude sufficient to modulate the band structure for ·OH generation. Significantly, the generation of electron–hole pairs on the surface through strain induction effectively addresses the unfavorable band alignment issue inherent in unstrained 3R-MoS_2 for photocatalytic applications.

The anisotropic compressive strain along armchair and zigzag orientations demonstrates enhanced redox capacity of 3R-MoS_2 toward HCHO degradation in photocatalytic systems. Mechanistic analysis revealed that the piezoelectric polarization induced by compressive deformation facilitates efficient hole-mediated water oxidation, with hydroxyl radicals predominantly localized at the piezopotential-induced h^+ accumulation regions. Notably, the characteristic lone-pair electron configuration of these transient

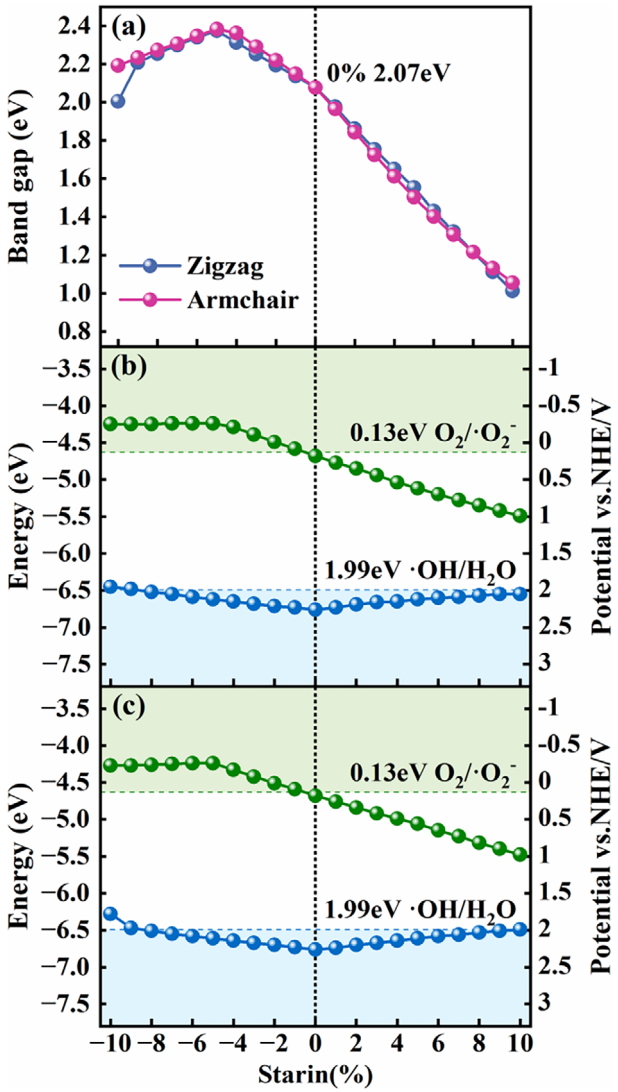

FIGURE 3 | (a) The calculated bandgaps of 3R-MoS_2 under varying strain ratios along the armchair and zigzag directions. Band edge positions of CBM and VBM of 3R-MoS_2 in (b) Armchair direction and (c) Zigzag direction under different strain ratios with $O_2/\cdot O_2^-$ and $\cdot OH/H_2O$ potentials.

hydroxyl species enables clear identification through electron paramagnetic resonance (EPR) spectroscopy, providing a robust experimental verification methodology for practical photocatalytic systems [9]. Moreover, the enhanced generation of hydroxyl radicals directly correlates with accelerated HCHO degradation kinetics, thereby improving overall degradation efficiency.

By analyzing the influence of deformation proportions on the band edge positions and intrinsic polarization of MoS_2 monolayers, we determined that a −6% compressive strain along the armchair orientation is optimal. Strain analysis revealed that this deformation shifts the CBM of 3R-MoS_2 from 0.18 to −0.26 eV, positioning it above the $O_2/\cdot O_2^-$ reduction potential (0.13 eV), thereby enhancing the thermodynamic feasibility of the oxygen reduction reaction (ORR). Meanwhile, the valence band maximum decreased from 2.26 to 2.09 eV but remains below the $\cdot OH/H_2O$ oxidation potential (1.99 eV), ensuring preserved photocatalytic activity for HCHO degradation. We therefore systematically evaluate the compressive strain effect ($\varepsilon = -6\%$) along the armchair axis on the HCHO decomposition kinetics below.

2.3 | Synergistic Piezo-Photocatalytic Mechanism of HCHO Oxidation on 3R-MoS_2

2.3.1 | The Adsorbed Species and Their Strain-induced Energetics on 3R-MoS_2

To decipher the atomistic mechanisms of HCHO photocatalytic oxidation on 3R-MoS_2, we systematically investigated the initial adsorption energetics of reactants and key intermediates at the gas–solid interface, with particular emphasis on piezoelectric potential-modulated surface interactions. Herein, the behavior of HCHO and ·OH onto MoS_2 were first quantified. Our systematic investigation of HCHO adsorption on 3R-MoS_2 surfaces revealed two distinct adsorption geometries through DFT calculations (Figure S2). The parallel orientation, characterized by η^2(C,O)-MoS_2 coordination with a 3.00 Å interface distance, demonstrated 0.30 eV physisorption energy via van der Waals interactions. In contrast, the perpendicular configuration exhibited weaker binding (0.02 eV) due to the reduced orbital overlap. The energetics were calculated via Equation S1, confirming surface physisorption dominance with configuration-dependent stabilization. Accordingly, the relatively stable parallel adsorption configuration was adopted in this study to establish and validate the reaction pathways for HCHO degradation.

Notably, hydroxyl radical adsorption displayed fundamentally different behavior, showing 1.00 eV chemisorption energy through covalent S—O bonding of 1.95 Å (Figure S3). Such threefold enhancement compared to HCHO adsorption originates from the radical's unpaired electron participation in interfacial charge transfer, as quantified by the following density of states analysis. Moreover, the mechanochemical response under 6% armchair direction compressive strain in 3R-MoS_2 revealed strain-insensitive ·OH adsorption ($\Delta E_{ads} < 0.01$ eV), while HCHO adsorption energy increased to 0.31 eV. These findings reveal that strain engineering predominantly modifies the catalyst's electronic environment rather than altering its intrinsic surface adsorption behavior.

To elucidate the mechanism of piezo-photocatalytic HCHO oxidation at the atomic scale, we performed DFT calculations to determine the reaction free energies and key intermediate transition states for HCHO oxidation on MoS_2 monolayer under 0% and −6% strain along armchair orientation (Figure 4; Figure S4). The reaction pathway, initiated by ·OH radical and HCHO co-adsorption, bifurcates into dual pathways through four primary steps as below:

1. $HCHO^* + {}^*\cdot OH \rightarrow {}^*CHO + H_2O^*$ (TS1)
2. $^*CHO + {}^*\cdot OH \rightarrow {}^*HCOOH$
3. $^*HCOOH + {}^*\cdot OH \rightarrow H^+ + H_2CO_3^*$ (TS2) or $^*HCOOH + {}^*\cdot OH \rightarrow HCOO^* + H_2O^*$ (TS4)
4. $H_2CO_3^* \rightarrow H_2O^* + {}^*CO_2$ (TS3) or $HCOO^* + {}^*\cdot OH \rightarrow H_2O^* + {}^*CO_2$ (TS5)

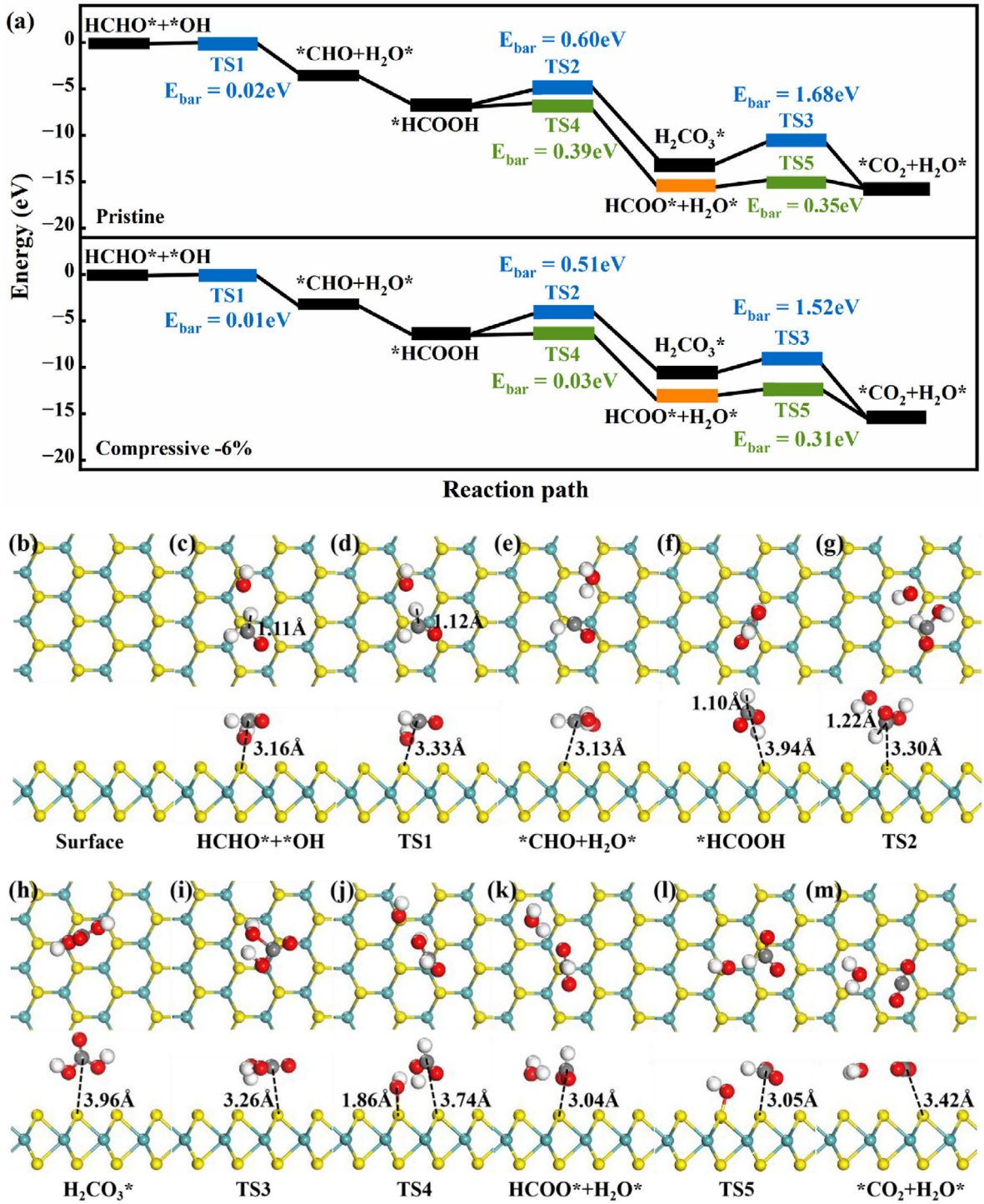

FIGURE 4 | (a) Reaction pathways of HCHO photocatalytic oxidation on pristine and strain-modulated 3R-MoS_2 (001) surfaces; (b–m) The calculated TS and intermediate structures for HCHO photocatalytic oxidation on −6% armchair-oriented strained 3R-MoS_2 (001) surface.

2.3.2 | Piezoelectric Optimization of Photocatalytic HCHO Oxidation Pathways

Through a multiscale approach combining spin-polarized DFT calculations and microkinetic modeling, we unraveled the -6% strain-modulated reaction coordinates of HCHO oxidation as well as on the non-polarized 3R-MoS_2 monolayer (Figure 4; Figure S4), initiating from the ·OH/HCHO co-adsorption phase. The calculated co-adsorption free energy (1.39 eV) demonstrated by stabilization 0.09 eV compared to the sum of individual adsorption energies.

During the initial dehydrogenation of HCHO (step 1), an H atom from the adsorbed HCHO* transferred to a neighboring *·OH, yielding *CHO and H_2O*. Transition state analysis (TS1) for C—H bond cleavage revealed a minimal elongation of the bond length on the non-polarized 3R-MoS_2 monolayers (as illustrated in Figure S4c, 1.11 Å → 1.14 Å). This structural distortion aligned

with the low energy barrier identified in subsequent calculations, confirming the reaction's facile kinetics. Similarly, under −6% armchair-oriented piezoelectricity (Figure 4d), the C—H bond stretched marginally from 1.11 to 1.12 Å, with the hydrogen atom remaining proximate to the ·OH group irrespective of stress. Notably, both systems (0% and −6% piezoelectricity) exhibited virtually identical dehydrogenation energies (∼3.96 eV) and extremely low energy barriers (0.02 eV vs. 0.01 eV). These results confirmed that the initial HCHO dehydrogenation step is thermodynamically and kinetically insensitive to external polarization forces.

In Step 2, *CHO reacts with *·OH, where the C atom in *CHO bonds with the O atom in *·OH to form *HCOOH, releasing approximately 3.80 eV of energy under both 0% and −6% strain conditions. Subsequent reactions on the MoS_2 monolayer proceeded via two distinct Routes: Route 1: *HCOOH + *·OH → H_2CO_3* → H_2O* + *CO_2; Route 2: *HCOOH + *·OH → HCOO* → H_2O* + *CO_2.

The transition state TS2 for Step 3 in Route 1 was identified, with the 0% and -6% strain systems as illustrated in Figure S4f and Figure 4g, respectively. The transition state geometries of the two systems exhibited significant structural divergences under these conditions. For the 0% strain system, the TS2 structure closely resembles H_2CO_3 in geometry and requires overcoming a high energy barrier of 0.60 eV. In contrast, under −6% strain, interfacial restructuring manifests critical geometrical alterations versus the unstressed system with the HCOOH-surface distance contracting significantly from 3.94 to 3.30 Å, indicating enhanced interfacial interaction. Moreover, the C—H bond in HCOOH underwent 0.12 Å elongation suggesting bond activation and approaching reactive proximity. These synergistic structural changes collectively reduce the reaction energy barrier to 0.51 eV, demonstrating stress-induced catalytic enhancement through optimized molecular orientation and electronic state modification. In Step 4 involving H_2CO_3 hydrolysis to H_2O and CO_2, comparative energy barrier analysis reveals persistent kinetic challenges across systems while the activation energy barrier marginally decreases from 1.68 eV (0% strain) to 1.52 eV (−6% strain), yet remains thermodynamically unfavorable despite applied compressive strain.

Intriguingly, comparative pathway analysis revealed mechanistic predominance of Route 2 in HCHO degradation, with TS4 (0.39 eV) and TS5 (0.35 eV) barriers being 35% and 79% lower than their Route 1 counterparts (TS2: 0.60 eV, TS3: 1.68 eV), conclusively establishing the HCOO-intermediate pathway as the thermodynamically favored route on MoS_2 surfaces regardless of polarization states. Kinetic analysis reveals that Step 3 emerges as the rate-determining bottleneck with an activation barrier of 0.39 eV in Route 2. The TS4 intermediate maintains a formic acid-like (HCOOH) configuration on both pristine and compressively strained (−6%) surfaces, with the interfacial *·OH-surface distance exhibiting a contraction from 2.06 to 1.86 Å under strain. This geometric compression demonstrates enhanced adsorption proximity and strengthened interfacial interactions induced by mechanical strain. Remarkably, compared to the high energy barrier in TS2 caused by bond-length stretching during H_2CO_3* formation, the strain–shortened interface distance in TS4 effectively lowers the barrier, demonstrating selective catalytic enhancement governed by strain-induced electronic restructuring and geometric confinement effects.

Systematic analysis demonstrates that −6% compressive strain engineering induces concerted catalytic enhancement in the HCHO degradation pathway, achieving a reduction in each elementary reaction barrier through strain-modulated surface restructuring, while maintaining exothermic thermodynamics. The HCOOH intermediate critically governs HCHO degradation kinetics through strain-modulated bifurcated pathways, with pathway being enabled selective acceleration of the HCOO-mediated dehydrogenation route. Crucially, −6% armchair-direction strain selectively reduces the rate-determining step barrier from 0.39 to 0.03 eV (Δ = −92%), establishing strain-engineered MoS_2 as a high-performance photocatalyst for complete HCHO mineralization through a HCOO-mediated pathway. More significantly, a −6% armchair-oriented external deformation not only effectively reduces the energy barrier of the elementary reaction but also alters the rate-determining step of the reaction, thereby enhancing the overall degradation efficiency.

2.3.3 | Structural Characterization and Experimental Verification of the Piezoelectric-Catalytic Performance of 3R-MoS_2

We began by synthesizing 3R-MoS_2 and the mechanically exfoliated few-layer samples exhibited clear optical contrast with the substrate (Figure 5a). Two dominant Raman peaks are observed at 380 and 405 cm^{-1} in multilayer 3R-MoS_2, corresponding to the in-plane vibrations of Mo and S atoms (mode) and the out-of-plane vibrations of S atoms (mode), respectively [45]. The frequency difference (Δ ≈25 cm^{-1}) between these peaks confirms the multilayer nature of the sample (Figure 5b). Furthermore, Raman mapping revealed spatially uniform intensity distributions for all major vibrational modes (Figure 5c), indicating high crystalline and excellent compositional homogeneity within the mechanically exfoliated nanoflakes.

Systematic second-harmonic generation (SHG) measurements conducted on the as-synthesized MoS_2 flakes confirmed their non-centrosymmetric crystal structure, which is a fundamental prerequisite for piezoelectricity that enables electric charge generation under mechanical deformation. Upon excitation with a 1050 nm femtosecond laser, a sharp SHG peak emerged at 525 nm (Figure 5d), a signature exclusive to materials lacking inversion symmetry. Spatially resolved SHG mapping further revealed regional variations in nonlinear response, likely due to differences in thickness, defect density, or crystal orientation, suggesting that piezoelectric polarization under strain may exhibit spatial heterogeneity, with high-intensity regions (shown in red in Figure 5e) displaying irregular morphology. Importantly, the observed six-fold SHG pattern (Figure 5f) matches the predicted sixfold rotational symmetry response for trigonal prismatic MoS_2 (e.g., trilayer 3R or monolayer phases), providing unambiguous evidence of threefold rotational symmetry and the broken inversion symmetry in the 3R-MoS_2 sample.

Moreover, our findings not only confirm the existence of piezoelectricity but also reveal its anisotropic nature. Figure 5g

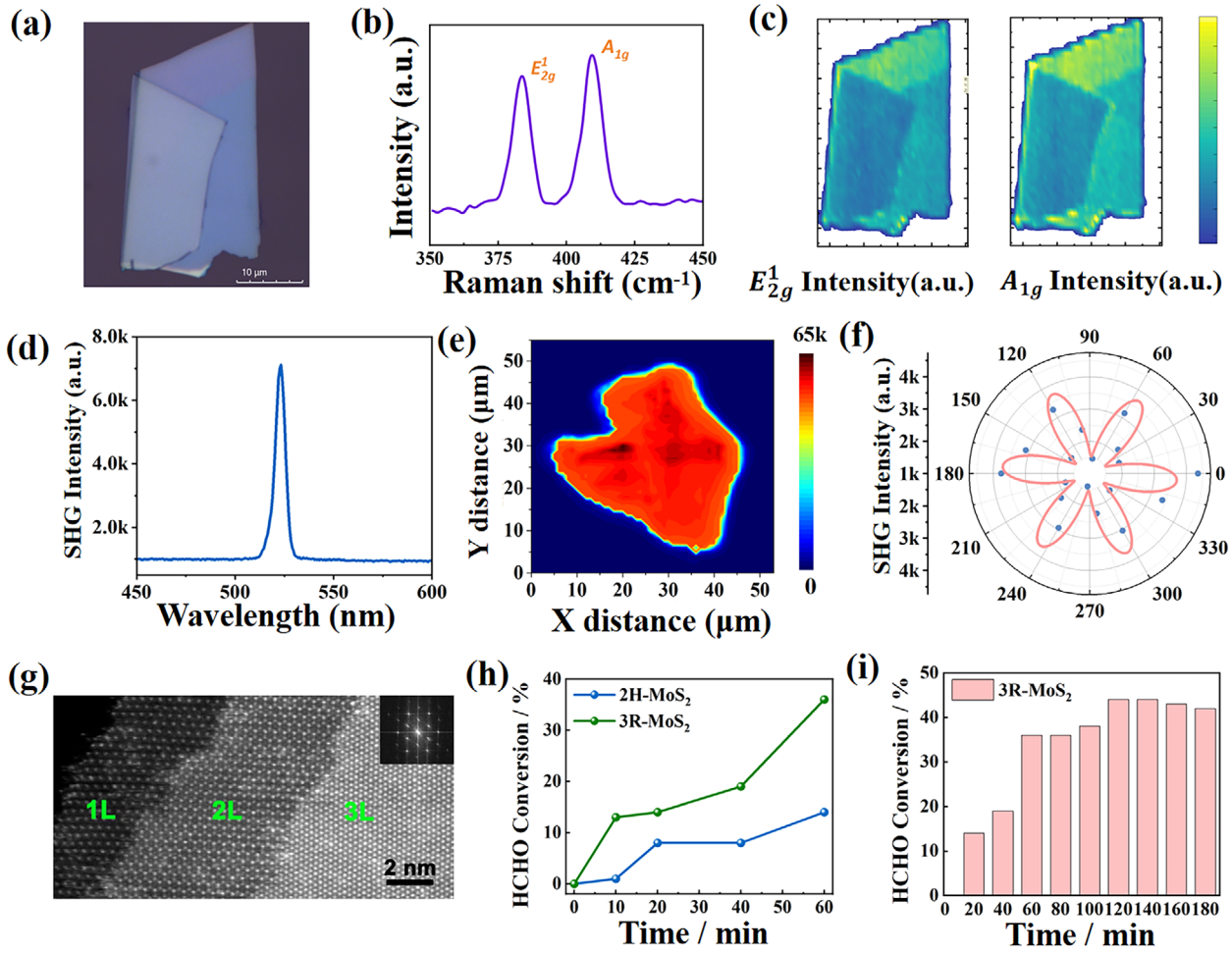

FIGURE 5 | (a) Optical microscope image of mechanically exfoliated MoS_2 thin sheets (scale bar: 10 μm). (b,c) Typical Raman spectrum of multilayer MoS_2 acquired under 532 nm laser excitation. (d) Second-harmonic generation (SHG) intensity as a function of excitation wavelength. (e) 2D spatial mapping of SHG intensity across the flake surface. (f) The polar coordinate diagram of the second harmonic intensity varying with the laser polarization Angle. (g) Cross-sectional high-resolution scanning transmission electron microscopy (HR-STEM) image with corresponding atomic structure models (right). (h) Comparative formaldehyde degradation performance of 3R-MoS_2 and 2H-MoS_2. (i) Catalytic robustness of 3R-MoS_2 evaluated over 180 min.

provides atomic-scale evidence of the layer-dependent stacking structure in MoS_2 flakes, with regions of one, two, and three atomic layers clearly labeled as 1L, 2L, and 3L, respectively. The selected-area electron diffraction (SAED) pattern in the inset shows sharp hexagonal diffraction spots, indicating hexagonal symmetry in the atomic arrangement and confirming that the 3R-MoS_2 flakes consist of single-crystalline domains [46]. The catalytic performance of 3R-MoS_2 was evaluated through formaldehyde degradation under ultrasonic irradiation (Figure 5h). Using a 10 ppm formaldehyde solution, the degradation rate was observed to increase continuously with time. Remarkably, 3R-MoS_2 achieved a degradation rate more than twice that of the 2H phase within 60 min, demonstrating markedly enhanced activity and stability. This superior performance was sustained over extended operation, with the material retaining significant degradation capability after 120 min in a 180-min test (Figure 5i), underscoring its practical application potential. In addition, the critical role of ·OH was also verified experimentally using a radical scavenger (terephthalic acid, TA), which suppressed formaldehyde degradation efficiency to only 8%. This result provides direct evidence that the enhanced ·OH production, driven by piezoelectric polarization induced lattice strain, is indispensable for improving photocatalytic performance. To distinguish the individual contributions of ultrasonic-driven piezoelectric catalysis and conventional photocatalysis from their synergistic effect, control experiments were performed using 3R-MoS_2 under either light-only or ultrasound-only conditions. As shown in Figure S5, the formaldehyde degradation efficiency remained below 10% in both cases, indicating that neither individual photocatalysis nor ultrasonic-driven piezoelectric catalysis can achieve the high degradation efficiency observed under the ultrasonic-light coupled condition. This confirms that the previously observed enhancement in degradation efficiency is indeed attributable to the synergistic interplay between the piezoelectric and photocatalytic effects in 3R-MoS_2.

2.3.4 | Atomistic Origins of Piezocatalytic Enhancement in HCHO Oxidation on 3R-MoS_2

To elucidate the mechanism by which piezoelectric effects enhance HCHO oxidation, we first comprehensively examined the adsorption behaviors of pristine and piezoelectrically strained

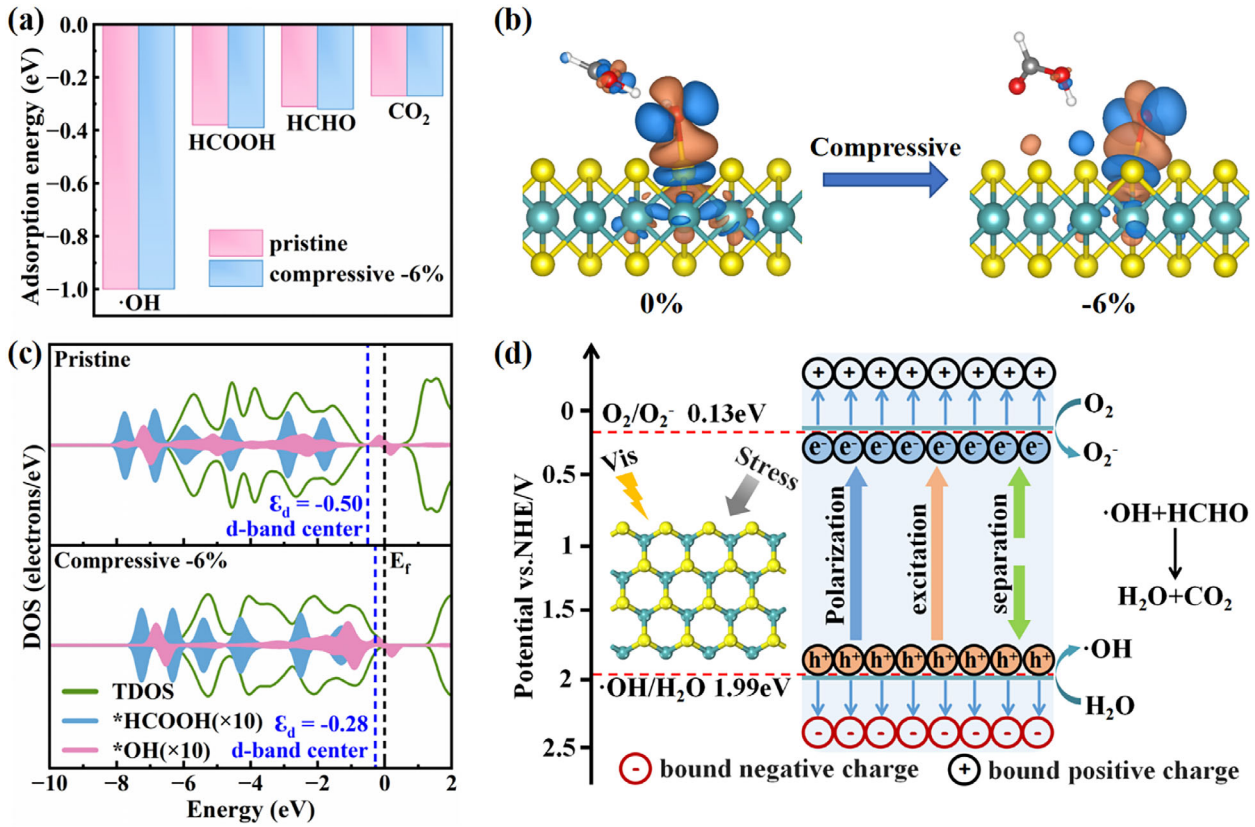

FIGURE 6 | (a) Adsorption behaviors of reactive species on pristine and −6% MoS_2 (001) surface; (b) Charge density difference plot for the co-adsorption system of *HCOOH and *·OH onto pristine and −6% armchair-oriented strained MoS_2 (001) surface. Blue and orange represent areas of electron accumulation or lack, respectively. The isosurface is set to 2.00×10^{-3} e/Å^3; (c) the total density of states and projected density of states for the co-adsorption system of *·OH and *HCOOH on pristine and −6% armchair-oriented strained MoS_2 (001) surface. The Fermi level is set to be zero, shown by the black dashed lines; (d) Schematic diagram of piezoelectric-photocatalytic synergistic mechanism for HCHO oxidation on 3R-MoS_2.

(−6% compression) MoS_2 toward critical species including reactants (·OH radical and HCHO), key intermediates (HCOOH, HCHO), and the final product CO_2. As shown in Figure 6a, theoretical calculations indicate negligible piezoelectric-induced enhancement in the intrinsic adsorption capacity of MoS_2 for these chemical entities. Interestingly, detailed analysis of the predominant reaction pathway reveals that piezoelectrically induced lattice strain fundamentally alters the co-adsorption geometry of HCOOH and ·OH radical. This alteration in synergistic adsorption patterns may optimize the spatial arrangement and charge distribution of reaction intermediates, thereby influencing the activation energy barriers in subsequent oxidation processes.

Accordingly, an in-depth examination was conducted on the charge density difference (Figure 6b) and density of states (Figure 6c) for the co-adsorption system of *·OH and *HCOOH on both surfaces, where the distinct electronic interaction characteristics were revealed. Comparative observations demonstrated that the compressed MoS_2 surface with −6% strain exhibited significantly enhanced electron redistribution phenomena compared to its pristine counterpart. Specifically, the interfacial regions between *·OH and the strained MoS_2 surface displayed more pronounced electron accumulation and depletion features, indicative of intensified charge transfer dynamics. This amplified electronic interaction under compressive strain correlates with the observed enhancement in surface reactivity, suggesting that lattice strain engineering effectively modulates the charge exchange processes at the catalyst–adsorbate interface. The strain-induced electronic structure modification provides a plausible explanation for the improved catalytic performance demonstrated in the reaction system.

The projected density of states (PDOS) analysis revealed critical electronic modifications induced by compressive strain in the co-adsorption system. Notably, *HCOOH and *·OH species on the −6% compressed MoS_2 exhibited distinct energy level alignment, with their occupied states positioned closer to the Fermi level as compared to those on pristine MoS_2. Such energy shift is particularly pronounced for *OH, which shows significantly enhanced electron density near the Fermi level under compressive strain. The total density of states (TDOS) of the strained MoS_2 system displays a marked upward shift toward the Fermi level relative to the pristine MoS_2 monolayer, consistent with enhanced surface reactivity. In addition, the calculated d-band center positions (−0.50 eV for pristine vs. −0.28 eV for −6% strained MoS_2, marked by blue dashed lines in Figure 6c) demonstrated that compressive strain induces a systematic upward shift of the d-band, effectively narrowing the energy gap between the active orbitals of MoS_2 and adsorbate frontier states. This demonstrates that the upward shift in the d-band center arises predominantly from strain-induced electron redistribution, not merely from geometric effects. Such electronic structure modulation correlates with the observed

catalytic enhancement, as the closer proximity of the d-band center to the Fermi level facilitates stronger orbital hybridization and charge redistribution during the reaction process, which is consist with previous literatures [47].

Our mechanistic investigations elucidated the piezoelectric-photocatalytic HCHO degradation pathway in 3R-MoS_2 (Figure 6d), where the synergy between light excitation and piezoelectric polarization establishes an efficient reaction system. The piezoelectric-induced lattice strain enabled band structure optimization through orbital energy level modulation, facilitating effective photoexcitation of charge carriers from valence band (VB) to conduction band (CB) under illumination. Concurrently, the strain-modified VB configuration enhances water oxidation kinetics through optimized hole accumulation, promoting efficient generation of ·OH for HCHO decomposition. The complete mineralization pathway proceeds through sequential oxidation steps: HCHO → CO_2 + H_2O, enabled by the sustained radical production. Crucially, the intrinsic piezoelectric field in monolayer 3R-MoS_2 creates directional charge transport channels, achieving enhanced directional migration and spatial separation of photogenerated electron–hole pairs. This dual-function system combines strain-engineered electronic states for enhanced carrier generation with built-in electric fields to suppress recombination, synergistically boosting catalytic performance through piezoelectric-optical energy conversion.

3 | Conclusion

In conclusion, this study demonstrates strain-engineered piezoelectric enhancement in non-centrosymmetric 3R-phase MoS_2 monolayers through DFT calculations, while elucidating the atomic-scale coupling mechanism between piezoelectric polarization and photocatalytic processes for synergistic HCHO degradation. The 3R phase demonstrates comparable stability to conventional 2H-MoS_2 while exhibiting unique strain-responsive electronic behavior, i.e., −6% armchair compression induces anisotropic bandgap widening (2.07→2.35 eV) and band edge shifts, precisely aligning with critical redox potentials of ·OH/H_2O and O_2/·O^{2-} for enhanced charge separation. Crucially, the piezoelectric polarization mechanism displays strain-dependent anisotropy through Born effective charge-lattice distortion coupling. Armchair-oriented compression (−10%) generates substantial spontaneous polarization (−0.14 C/m^2) via cumulative vector superposition of asymmetric Mo—S displacements with enhanced charge transfer (Mo = 1.58 e, S = −0.78 e), while tensile strain induces charge neutralization and zigzag-directional loading yields negligible polarization (Ps ≈0 C/m^2). Through synergistic optimization of photonic absorption and piezoelectric response, the system achieves maximum catalytic efficiency under −6% armchair compression, effectively reducing critical energy barriers in the thermodynamically preferred HCOO* oxidation pathway from 0.39 eV (pristine) to 0.03 eV for the rate-determining step. These findings provide atomic-level insights into lattice strain-modulated 3R-MoS_2 catalysts, establishing a multiscale framework for designing coupled piezoelectric–photocatalytic systems with enhanced environmental remediation capabilities.

4 | Computational Simulation and Experimental Verification

4.1 | Global Phase Screening of MoS_2 With Stochastic Surface Walking Algorithm

Utilizing the global optimization capabilities of the stochastic surface walking (SSW) method [48], we explored the potential energy surface (PES) of the MoS_2 phase space through neural network (NN) potentials autonomously trained on first-principles-derived global PES datasets. This NN potential was constructed through our previously developed SSW-NN framework [48], which implements a "global-to-global"strategy to ensure comprehensive PES coverage and quantum-mechanical accuracy. Such SSW-NN approach accelerates PES sampling by over four orders of magnitude while maintaining fidelity comparable to the first-principles calculations [49]. The SSW-NN methodology enables exhaustive and unbiased sampling of the complex PES of MoS_2, revealing previously elusive transient microstructures through its enhanced configurational exploration capabilities.

To project the multidimensional PES into a 2D visualization (energy vs. structural geometry), we adopted a distance-weighted Steinhardt-type order parameter (OP) [50] for quantifying atomic configurations, with the OP values mapped to the x-axis in Figure 1d. The y-axis represents the energy per formula unit (f.u.), with the energy zero point established at the energy zero point of the global minimum (GM) (MoS_2-2H phase). The OP is written as:

$$\mathrm{OP}_l = \left(\frac{4\pi}{2l+1} \sum_{m=-l}^{l} \left| \frac{1}{N_{\mathrm{bonds}}} \sum_{i \neq j} e^{-\frac{1}{2}\frac{r_{ij}-r_c}{r_c}} Y_{lm}(n) \right|^2 \right)^{\frac{1}{2}} \quad (1)$$

where Y_{lm} is the spherical harmonic function; i and j are the atoms in lattice; r_{ij} is the distance between atoms i and j; r_c is set as 60% of the typical single bond length between i and j atoms; N_{bonds} is the number of bonds in the first bonding shell; the degree is set as 2 (OP_2) [49, 51].

4.2 | DFT Modeling of Gas–Solid Interface Chemistry in 3R-MoS_2

All DFT calculations were performed using the Vienna Ab initio Simulation Package (VASP) with a dual-functional approach to ensure both computational efficiency and accuracy. Structural optimizations were performed using the Perdew–Burke–Ernzerhof (PBE) generalized gradient approximation (GGA) functional to accurately refine atomic coordinates and lattice parameters, while subsequent high-precision electronic structure evaluations were performed with the Heyd–Scuseria–Ernzerhof (HSE06) hybrid functional [52]. A plane-wave cutoff energy of 400 eV was employed to ensure accurate representation of electronic states and pseudopotentials for all elements (C, H, O, S, Mo) in the adsorption system. Structural relaxations were considered to be converged when atomic forces dropped below 0.02 eV/Å, with van der Waals (vdW) interactions between adjacent layers explicitly incorporated through the DFT-D3 dispersion correction method. The (001) facet of the 3R-MoS_2 crystal was

used to construct a 4 × 4 × 1 supercell surface, forming a monolayer structure comprising 48 atoms (16 Mo and 32 S) with stoichiometric consistency, as illustrated in Figure 1e. To better simulate the effects of interlayer interactions, we included a vacuum layer with a height of 20 Å [53] in the monolayer 3R-MoS_2 construction to reduce errors. The photocatalytic degradation pathway of HCHO on monolayer 3R-MoS_2 was systematically investigated using the Nudged Elastic Band (NEB) method within transition state theory, with the minimum energy path determined from pre-optimized reactant and product configurations. Detailed calculations of the adsorption energies and reaction energy barriers for the system can be found in the Supporting Information (SI).

4.3 | Multiscale Evaluation of Piezoelectricity and Optical Response in 3R-MoS_2

MoS_2, a prototypical 2D material, has garnered substantial interest for its exceptional properties and potential in nanoelectronics, photonics, and sensing. Its non-centrosymmetric structure (D_3h point group) endows it with a piezoelectric effect, characterized by a single independent piezoelectric coefficient. The relevant e coefficient is defined by the following relation:

$$e_{111} = e_{11}$$

$$e_{122=}\, e_{12=} \; - e_{11}$$

$$e_{212} = e_{221} = e_{26} = -e_{11} \tag{2}$$

The matrix form of the piezoelectric e tensor is:

$$e_{3\times6} = \begin{Bmatrix} e_{11} & -e_{11} & 0 & 0 & 0 & 0 \\ 0 & 0 & 0 & 0 & 0 & -e_{11} \\ 0 & 0 & 0 & 0 & 0 & 0 \end{Bmatrix} \tag{3}$$

Accordingly, we employed constitutive thermodynamic equations to resolve the strain-dependent spontaneous polarization in piezoelectric 3R-MoS_2 along high-symmetry directions, with its anisotropic response under uniaxial/biaxial strain and strain ratio quantitatively described by:

$$\Delta \mathrm{P} \; = \frac{e}{\Omega} \sum_{j\beta} Z^{*}_{\mathrm{j}\alpha\beta} \Delta\mu_{\mathrm{j}\beta} \tag{4}$$

where $Z^{*}_{\mathrm{j}\alpha\beta}$ represents the Born effective charge tensor of the system; Ω denotes the volume of the crystal cell; $\Delta\mu_{\mathrm{j}\beta}$ indicates the atomic shift of each atom in the system relative to the centrosymmetric phase; e refers to the charge magnitude of an electron, which is 1.6×10^{-19} C. The subscript refers to the corresponding atomic serial number in the symmetric system structure and non-centrosymmetric structure.

The precise determination of valence band maximum (VBM) and conduction band minimum (CBM) positions plays a critical role in assessing photocatalytic performance, as these parameters govern the material's redox capability. These essential electronic characteristics are derived from comprehensive computational analysis of band structure eigenvalues combined with vacuum level alignment and bandgap energy considerations. The calculation formulas of band positions are as follows:

$$E_{\mathrm{VBM}}\,(eV) = E_{\mathrm{VB}} \; - E_{\mathrm{vacuum}} - E_{\mathrm{NHE}} \tag{5}$$

$$E_{\mathrm{CBM}}\,(eV) = E_{\mathrm{VBM}} + E_{\mathrm{g}} \tag{6}$$

where E_{VB} denotes the semiconductor valence band eigenvalue; E_{vacuum} is the vacuum level; E_{g} is the bandgap (all at given strain ratios); and E_{NHE} represents the hydrogen-referenced energy level (4.5 eV). $E_{\mathrm{VBM/CBM}}$ is the oxidation-reduction potential of the 3R-MoS_2 substrate at pH 7.

4.4 | Experimental Synthesis and Characterization

In the experimental verification section, 3R MoS_2 single crystals were synthesized via chemical vapor transport (CVT) using $MoCl_5$ as the transport agent. Stoichiometric amounts of Mo (powder, 99.99%), S (powder, 99.99%), and $MoCl_5$ (powder, 99.99%) in a 9:20:1 molar ratio, with a total mass of 500 mg, were sealed in a 20 cm long quartz tube under a vacuum of 10^{-6} Torr. The sealed tube was placed in a three-zone furnace and subjected to a pretreatment at 850°C for 30 h, while the growth zone was held at 920°C to prevent premature sample transport. Subsequently, the reaction zone was heated to 1080°C, with the growth zone maintained at 920°C for 6 days to establish a temperature gradient conducive to single crystal growth. Finally, the furnace was cooled naturally to room temperature, and 3R MoS_2 single crystals were collected from the growth zone.

The structural characterization involved comprehensive Raman spectroscopy and second-harmonic generation (SHG) measurements. Raman spectroscopy and Raman Mapping data were acquired using a HORIBA Xplora Plus system, employing a 532 nm laser wavelength. To prevent any damage to the sample, the laser power was meticulously maintained at less than 100 μW, and the acquisition time was set to 60 s. A 100x objective lens and a 1200 lines mm^{-1} grating was utilized, which provided a spectral resolution of less than 1.6 cm^{-1}. The Raman peaks at 380 and 405 cm^{-1}, corresponding to in-plane (E_{2g}) and out-of-plane (A_{1g}) vibrational modes, respectively, with a difference $\Delta \approx 25$ cm^{-1}, confirmed the multilayer nature of the samples. For SHG measurements, the output from a Ti:sapphire femtosecond laser (Chameleon Ultra I, Coherent) was guided through reflective optics and tightly focused via a 100x microscope objective (spot size ~1.3 μm at 850 nm). The emitted SHG signal was collected in the backward direction through the same objective, isolated by a dichroic mirror, and purified with a short-pass filter before spectral analysis using a high-sensitivity spectrometer (TuoTuo Technology, TTT-03-SHG).

The photocatalytic performance was evaluated by means of formaldehyde degradation experiments conducted using the

phenol reagent spectrophotometric method. In brief, 100 mg of either 3R-MoS_2 or 2H-MoS_2 catalyst was introduced into 40 mL of a 10 ppm HCHO solution, which was then sealed and subjected to ultrasonic irradiation at a controlled temperature of 23°C±2°C. At predetermined time intervals (e.g., 0, 1, 7, 10, 15, 20, 30, 40, 50, and 60 min), aliquots of 100 μL were withdrawn, mixed with 4.9 mL of phenol reagent absorption solution, and combined with 0.4 mL of 1% ammonium iron (III) sulfate color developer. It is noted that ambient natural light served as the light source for the photocatalytic experiments. The mixtures were subsequently incubated in the dark for 15 min. Absorbance was measured at 630 nm using a 1 cm quartz cuvette, and the HCHO concentration was determined based on a pre-established calibration curve.

Acknowledgements

This work was supported by the Introduction Innovative and Research Teams Project of Guangdong Pearl River Talents Program (2023ZT10L102), the National Natural Science Foundation of China (22576040, 42377221, 42577034), the Natural Science Foundation of Guangdong Province (2019A1515010428), and the Guangzhou Science and Technology Project (202102020126).

Conflicts of Interest

The authors declare no conflicts of interest.

Data Availability Statement

The data that support the findings of this study are available in the supplementary material of this article.

References

1. J. Y. Zheng, C. X. Liu, C. B. Han, et al., "Electrostatically Induced Non-Uniform Surface Charges Enhancing HCHO Catalytic Oxidation Based on Elastic Sponge Catalyst," *Advanced Functional Materials* 35 (2025): 2416004.

2. S. Gaur, S. Singh, J. Deb, et al., "Site-Selective MoS_2 -Based Sensor for Detection and Discrimination of Triethylamine From Volatile Amines Using Kinetic Analysis and Machine Learning," *Advanced Functional Materials* 34 (2024): 2405232.

3. Y. Nunez, J. Benavides, J. A. Shearston, et al., "An Environmental Justice Analysis of Air Pollution Emissions in the United States From 1970 to 2010," *Nature Communications* 15 (2024): 268.

4. X. L. Zhao, X. L. Wang, J. He, et al., "Time to Strengthen the Governance of New Contaminants in the Environment," *Nature Communications* 16 (2025): 7775.

5. Y. Y. Fan, W. C. Zhou, X. Y. Qiu, et al., "Selective Photocatalytic Oxidation of Methane by Quantum-Sized Bismuth Vanadate," *Nature Sustainability* 4 (2021): 509–515.

6. X. H. Liu, T. Lu, X. G. Jiao, et al., "Formaldehyde Ambient-Temperature Decomposition Over Pd/Mn_3O_4 –MnO Driven by Active Sites′ Self-Tandem Catalysis," *Environmental Science & Technology* 58 (2024): 1752–1762.

7. Y. J. Wan, X. Fan, and T. L. Zhu, "Removal of Low-Concentration Formaldehyde in Air by DC Corona Discharge Plasma," *Chemical Engineering Journal* 171 (2011): 314–319.

8. M. He, J. Ji, B. Y. Liu, and H. B. Huang, "Reduced TiO_2 With Tunable Oxygen Vacancies for Catalytic Oxidation of Formaldehyde at Room Temperature," *Applied Surface Science* 473 (2019): 934–942.

9. Z. Liang, C. F. Yan, S. Rtimi, and J. Bandara, "Piezoelectric Materials for Catalytic/Photocatalytic Removal of Pollutants: Recent Advances and Outlook," *Applied Catalysis B: Environmental* 241 (2019): 256–269.

10. S. K. Kuk, S. M. Ji, S. Kang, et al., "Singlet-Oxygen-Driven Photocatalytic Degradation of Gaseous Formaldehyde and its Mechanistic Study," *Applied Catalysis B: Environmental* 328 (2023): 122463.

11. Z. C. Wang, B. H. Di, S. Q. Gong, H. X. Li, Y. L. Min, and L. Zheng, "Piezoelectric Field and TENG Co-Promoted Photocatalytic Degradation of HCHO on $BaTiO_3$/g-C_3N_4/PTFE/Cu for Self-Cleaning and Air-Purification," *Applied Catalysis B: Environment and Energy* 364 (2025): 124859.

12. X. Y. Wang, J. Q. Meng, X. Y. Zhang, et al., "Controllable Approach to Carbon-Deficient and Oxygen-Doped Graphitic Carbon Nitride: Robust Photocatalyst Against Recalcitrant Organic Pollutants and the Mechanism Insight," *Advanced Functional Materials* 31 (2021): 2010763.

13. J. Q. Meng, X. Y. Wang, Y. Q. Liu, et al., "Acid-Induced Molecule Self-Assembly Synthesis of Z-Scheme WO_3/g-C_3N_4 Heterojunctions for Robust Photocatalysis Against Phenolic Pollutants," *Chemical Engineering Journal* 403 (2021): 126354.

14. W. Amdouni, M. Fricaudet, M. Otonicar, et al., "$BiFeO_3$ Nanoparticles: The "Holy-Grail" of Piezo-Photocatalysts?," *Advanced Materials* 35 (2023): 2301841.

15. Y. L. Guo, M. C. Wen, G. Y. Li, and T. C. An, "Recent Advances in VOC Elimination by Catalytic Oxidation Technology Onto Various Nanoparticles Catalysts: A Critical Review," *Applied Catalysis B: Environmental* 281 (2021): 119447.

16. Y. X. Deng, "Developing a Langmuir-Type Excitation Equilibrium Equation to Describe the Effect of Light Intensity on the Kinetics of the Photocatalytic Oxidation," *Chemical Engineering Journal* 337 (2018): 220–227.

17. H. Y. Yang, C. Z. He, L. Fu, et al., "Capture and Separation of CO_2 on BC_3 Nanosheets: A DFT Study," *Chinese Chemical Letters* 32 (2021): 3202–3206.

18. M. B. Starr, J. Shi, and X. D. Wang, "Piezopotential-Driven Redox Reactions at the Surface of Piezoelectric Materials," *Angewandte Chemie International Edition* 51 (2012): 5962–5966.

19. J. J. Wang, C. Hu, L. Shi, et al., "Energy and Environmental Catalysis Driven by Stress and Temperature-Variation," *Journal of Materials Chemistry A* 9 (2021): 12400–12432.

20. J. Yuan, X. Y. Huang, L. L. Zhang, et al., "Tuning Piezoelectric Field for Optimizing the Coupling Effect of Piezo-Photocatalysis," *Applied Catalysis B: Environmental* 278 (2020): 119291.

21. J. He, X. D. Wang, S. Y. Lan, et al., "Breaking the Intrinsic Activity Barriers of Perovskite Oxides Photocatalysts for Catalytic CO2 Reduction via Piezoelectric Polarization," *Applied Catalysis B: Environmental* 317 (2022): 121747.

22. Y. Chen, X. M. Deng, J. Y. Wen, J. Zhu, and Z. F. Bian, "Piezo-Promoted the Generation of Reactive Oxygen Species and the Photodegradation of Organic Pollutants," *Applied Catalysis B: Environmental* 258 (2019): 118024.

23. A. Ishag and Y. B. Sun, "Recent Advances in Two-Dimensional MoS_2 Nanosheets for Environmental Application," *Industrial & Engineering Chemistry Research* 60 (2021): 8007–8026.

24. U. Qamar, S. Roy, S. Kumar, et al., "Plasmonic Au_3 Cu Ordered Nanocrystals Induced Phase Transformation in 2D-MoS_2 for Efficient Hydrogen Evolution," *Advanced Functional Materials* 34 (2024): 2311943.

25. D. Tan, M. Willatzen, and Z. L. Wang, "Prediction of Strong Piezoelectricity in 3R-MoS_2 Multilayer Structures," *Nano Energy* 56 (2019): 512–515.

26. S. Li, Z. C. Zhao, J. Z. Zhao, Z. T. Zhang, X. Li, and J. M. Zhang, "Recent Advances of Ferro-, Piezo-, and Pyroelectric Nanomaterials for Catalytic Applications," *ACS Applied Nano Materials* 3, no. 2 (2020): 1063–1079.

27. W. Z. Wu, L. Wang, Y. L. Li, et al., "Piezoelectricity of Single-Atomic-Layer MoS_2 for Energy Conversion and Piezotronics," *Nature* 514 (2014): 470–474.

28. R. H. Liu, G. W. Hu, M. J. Dan, Y. M. Zhang, L. J. Li, and Y. Zhang, "Piezotronic Spin and Valley Transistors Based on Monolayer MoS_2," *Nano Energy* 72 (2020): 104678.

29. J. Shi, P. Yu, F. C. Liu, et al., "3R MoS_2 With Broken Inversion Symmetry: A Promising Ultrathin Nonlinear Optical Device," *Advanced Materials* 29 (2017): 1701486.

30. W. F. Cai, J. Y. Wang, Y. M. He, et al., "Strain-Modulated Photoelectric Responses From a Flexible α-In_2Se_3/3R MoS_2 Heterojunction," *Nano-Micro Lett* 13 (2021): 1838.

31. Y. M. Fu, Z. Q. Ren, J. Z. Wu, et al., "Direct Z-Scheme Heterojunction of ZnO/MoS_2 Nanoarrays Realized by Flowing-Induced Piezoelectric Field for Enhanced Sunlight Photocatalytic Performances," *Applied Catalysis B: Environmental* 285 (2021): 119785.

32. Z. Wang, Z. R. Liu, G. R. Zhao, et al., "Stretchable Unsymmetrical Piezoelectric $BaTiO_3$ Composite Hydrogel for Triboelectric Nanogenerators and Multimodal Sensors," *ACS Nano* 16 (2022): 1661–1670.

33. Y. F. Li, Z. Zhou, S. B. Zhang, and Z. F. Chen, "MoS_2 Nanoribbons: High Stability and Unusual Electronic and Magnetic Properties," *Journal of the American Chemical Society* 130 (2008): 16739–16744.

34. K. F. Mak, C. Lee, J. Hone, J. Shan, and T. F. Heinz, "Atomically Thin MoS_2: A New Direct-Gap Semiconductor," *Physical Review Letters* 105 (2010): 136805.

35. A. Splendiani, L. Sun, Y. B. Zhang, et al., "Emerging Photoluminescence in Monolayer MoS_2," *Nano Letters* 10 (2010): 1271–1275.

36. J. D. Zhou, J. H. Lin, H. Sims, et al., "Synthesis of Co-Doped MoS_2 Monolayers With Enhanced Valley Splitting," *Advanced Materials* 32 (2020): 1906536.

37. R. Suzuki, M. Sakano, Y. J. Zhang, et al., "Valley-Dependent Spin Polarization in Bulk MoS_2 With Broken Inversion Symmetry," *Nature Nanotechnology* 9 (2014): 611–617.

38. Y. Dong, M. M. Yang, M. Yoshii, et al., "Giant Bulk Piezophotovoltaic Effect in 3R-MoS_2," *Nature Nanotechnology* 18 (2023): 36–41.

39. M. J. Dai, W. Zheng, X. Zhang, et al., "Enhanced Piezoelectric Effect Derived From Grain Boundary in MoS_2 Monolayers," *Nano Letters* 20 (2020): 201–207.

40. F. Naunikin, P. Del Mazo-Sevillano, A. Aguado, Y. V. Suleimanov, and O. Roncero, "Zero- and High-Pressure Mechanisms in the Complex Forming Reactions of OH With Methanol and Formaldehyde at Low Temperatures," *ACS Earth and Space Chemistry* 3 (2019): 1158–1169.

41. M. A. Henderson and I. Lyubinetsky, "Molecular-Level Insights Into Photocatalysis From Scanning Probe Microscopy Studies on TiO_2 (110)," *Chemical Reviews* 113 (2013): 4428–4455.

42. K. Yokomizo and S. Murakami, "Non-Bloch Band Theory of Non-Hermitian Systems," *Physical Review Letters* 123 (2019): 066404.

43. K. Kawabata, N. Okuma, and M. Sato, "Non-Bloch Band Theory of Non-Hermitian Hamiltonians in the Symplectic Class," *Physical Review B* 101 (2020): 195147.

44. K. Ikeda, S. Aoki, and Y. Matsuki, "Hyperbolic Band Theory Under Magnetic Field and Dirac Cones on a Higher Genus Surface," *Journal of Physics: Condensed Matter* 33 (2021): 485602.

45. C. Lee, H. Yan, L. E. Brus, T. F. Heinz, J. Hone, and S. Ryu, "Anomalous Lattice Vibrations of Single- and Few-Layer MoS_2," *ACS Nano* 4 (2010): 2695–2700.

46. H. Hallil, W. F. Cai, K. Zhang, et al., "Strong Piezoelectricity in 3R-MoS_2 Flakes," *Advanced Electronic Materials* 8 (2022): 2101131.

47. V. R. Stamenkovic, B. Fowler, B. S. Mun, et al., "Improved Oxygen Reduction Activity on Pt 3 Ni(111) via Increased Surface Site Availability," *Science* 315 (2007): 493–497.

48. C. Shang and Z. P. Liu, "Stochastic Surface Walking Method for Structure Prediction and Pathway Searching," *Journal of Chemical Theory and Computation* 9 (2013): 1838–1845.

49. S. D. Huang, C. Shang, X. J. Zhang, and Z. P. Liu, "Material Discovery by Combining Stochastic Surface Walking Global Optimization With a Neural Network," *Chemical Science* 8 (2017): 6327–6337.

50. X. J. Zhang, C. Shang, and Z. P. Liu, "Pressure-Induced Silica Quartz Amorphization Studied by Iterative Stochastic Surface Walking Reaction Sampling," *Physical Chemistry Chemical Physics* 19 (2017): 4725–4733.

51. S. D. Huang, C. Shang, P. L. Kang, and Z. P. Liu, "Atomic Structure of Boron Resolved using Machine Learning and Global Sampling," *Chemical Science* 9 (2018): 8644–8655.

52. Y. M. Pu, Z. B. Qiu, B. Lv, et al., "The First-Principle Study On Certain Structural, Band-Structural, Elastic, Optical and Piezoelectric Properties of the Ca, Zr and Ca/Zr-doped $BaTiO_3$," *Modern Physics Letters B* 37 (2023): 2350007.

53. W. N. Zhao and Z. P. Liu, "Mechanism and Active Site Of Photocatalytic Water Splitting on Titania in Aqueous Surroundings," *Chemical Science* 5 (2014): 2256–2264.

Supporting Information

Additional supporting information can be found online in the Supporting Information section.

Supporting file: adfm73596-sup-0001-SuppMat.docx